International Journal of Thermal Sciences 225 (2026) 110805

Contents lists available at ScienceDirect

International Journal of Thermal Sciences

journal homepage: www.elsevier.com/locate/ijts

Infrared thermography-based estimation of Biot number in 2D polymeric fins using Levenberg–Marquardt and Gradient Boosting

Isabela Florindo Pinheiro [a,*], Debora Carneiro Moreira [b], Daniel Pereira Nunes Gama [a], Leandro Alcoforado Sphaier [a], Luiz Carlos da Silva Nunes [c]

[a] Department of Mechanical Engineering (TEM/PGMEC), Laboratory of Thermal Sciences (LATERMO), Universidade Federal Fluminense (UFF), Rua Passo da Pátria, nº 156, bloco E, room 206-D, São Domingos, Niteroi, CEP: 24.210-240, RJ, Brazil

[b] Department of Mechanical Engineering, Heat Transfer Research Group, São Carlos School of Engineering (EESC), University of São Paulo (USP), São Carlos, CEP: 13.566-590, SP, Brazil

[c] Department of Mechanical Engineering (TEM/PGMEC), Laboratory of Opto-Mechanics (LOM), Universidade Federal Fluminense (UFF), Rua Passo da Pátria, nº 156, bloco E, room 210-E, São Domingos, Niteroi, CEP: 24.210-240, RJ, Brazil

ARTICLE INFO

Keywords:
Infrared thermography
Integral transform
Inverse problem
Machine learning

ABSTRACT

This study combines experimental and theoretical approaches to investigate steady-state, multi-dimensional heat conduction in polymeric fins. Surface temperature fields are measured using infrared thermography, while a normalized two-dimensional heat conduction model is developed and solved via integral transform techniques. Two base boundary conditions — prescribed temperature (Dirichlet) and prescribed heat flux (Neumann) — are analyzed to evaluate their impact on thermal behavior and parameter estimation. The Biot number is estimated using two approaches: (1) an inverse problem solved with the Levenberg–Marquardt (LM) algorithm and (2) a machine learning model based on Gradient Boosted Trees (GBT). Synthetic data generated from the forward model serve as the training set for the GBT approach, aligning with Problem-Informed Machine Learning (PIML) methodologies. Both approaches are then employed to estimate the convective heat transfer coefficient, while the material's thermal conductivity is experimentally measured using a Heat Flow Meter (FOX 50). Results indicate that the LM method provides interpretability and strong performance when sensitivity is adequate and regularization is applied, while the GBT demonstrates greater robustness in nonlinear regimes and with ample training data.

1. Introduction

Infrared (IR) thermography has become an essential optical diagnostic technique in Engineering, particularly within the domain of Thermal Sciences. It is a non-destructive technique that enables the visualization of temperature distributions across object surfaces, offering significant advantages for experimental investigations. Over the past decades, a growing number of studies have explored the applications of IR thermography in Heat Transfer research, including convective heat transfer measurements around complex geometries [1], detection of internal defects in civil engineering structures such as concrete and masonry bridges [2], and even biomedical diagnostics, where dynamic infrared thermography has been employed to support the non-invasive identification of skin tumors [3]. Fundamentally, IR thermography operates by detecting infrared radiation naturally emitted by objects, which lies outside the visible spectrum detected by the human eye, specifically beyond wavelengths of approximately 700 nm. By employing specialized infrared cameras, this radiation is converted into a visible, computerized thermal image, allowing both qualitative and quantitative temperature measurements. In addition to being non-intrusive, infrared thermography offers high sensitivity, low response time, full two-dimensional data acquisition, and improved accuracy by minimizing errors associated with tangential conduction within the sensor [4], making it a powerful tool for both fundamental and applied thermal investigations.

The historical evolution and technological advances of infrared thermography, particularly in its application to heat transfer and fluid flow visualization, have been extensively documented by Carlomagno and Cardone [4] and Astarita et al. [1,5]. These works trace the development from the introduction of IR cameras in the 1960s (originally designed for military purposes) to the emergence of non-cooled Focal

* Corresponding author.
E-mail addresses: isabelaflorindo@id.uff.br (I.F. Pinheiro), dcmoreira@usp.br (D.C. Moreira), danielgama@id.uff.br (D.P.N. Gama), lasphaier@id.uff.br (L.A. Sphaier), luizcsn@id.uff.br (L.C.d.S. Nunes).

https://doi.org/10.1016/j.ijthermalsci.2026.110805
Received 28 July 2025; Received in revised form 24 January 2026; Accepted 27 February 2026
Available online 5 March 2026

Nomenclature

A	Integral Coefficients [−]
Bi	Biot number [−]
c_p	Specific heat at constant pressure $\left[\mathrm{J/kgK}\right]$
f	Unknown function [−]
h	Convective heat transfer coefficient $\left[\mathrm{W/m^2K}\right]$
H	Height [m]
J	Sensibility matrix [−]
k	Thermal conductivity $\left[\mathrm{W/mK}\right]$
L	Length [m]
N	Norms [−]
P	Parameter [−]
$\dot{q}''$	Heat flux $\left[\mathrm{W/m^2}\right]$
S	Objective function [−]
t	Time [s]
T	Temperature [K]
Y	Experimental/Simulated data [K]
Z	Eigenfunctions [−]
x, y, z	Spatial coordinates [m]

Greek Symbols

α	boundary condition factor [−]
δ	Thickness [m]
ϵ	Error [−]
γ	Aspect ratio [−]
μ	Eigenvalues [−]
ρ	density $\left[\mathrm{kg/m^3}\right]$
σ	Standard deviation [K]
Θ	Estimated dimensionless temperature [−]
θ	Dimensionless Temperature [−]
φ	General boundary condition parameter [−]
ξ, ζ	Dimensionless spatial coordinates [−]

Superscripts and Subscripts

av	average
b	base
exp	experimental
f	fluid
i	index associated with the predicted temperature
j	index associated with the measured/synthetic temperature
n, m	spatial indexes for truncation order
min	minimum
max	maximum
$*$	Dimensionless
$-$	Transformed
t	total

Abbreviations and Acronyms

CITT	Classical Integral Transform Technique
FPA	Focal Plane Array
GBT	Gradient Boosted Trees
GITT	Generalized Integral Transform Technique
IP	Inverse Problem
IR	Infrared
LM	Levenberg–Marquardt
MAE	Mean Absolute Error
ML	Machine Learning
MSE	Mean Squared Error
PDE	Partial Differential Equation
PIML	Physics-Informed Machine Learning
PINNs	Physics-Informed Neural Networks

Plane Array (FPA) thermal detectors, such as microbolometers, in the 1990s, which marked a major shift toward more accessible, sensitive, and complex imaging systems. As infrared thermography matured technologically, its applications expanded beyond traditional heat transfer visualization to encompass a broader range of fields. Notably, in civil engineering, Balaras and Argiriou [6] enumerates the use of thermal infrared imaging for identifying structural anomalies, estimating potential energy savings, scheduling interventions, and prioritizing preventive maintenance actions. For the last few years, the technique has gained increasing relevance in the study of polymeric materials, where its ability to capture detailed thermal responses has been particularly valuable. Measurement accuracy in these contexts can be influenced by several factors, including surface emissivity, atmospheric attenuation, ambient temperature fluctuations, wind conditions, and sensor–target distance [7]. Beyond qualitative inspections, infrared thermography has been successfully employed for quantitative analysis and material parameter estimation. For instance, Moslemi et al. [8] conducted a thermal response analysis of additively manufactured polymers, using infrared measurements to predict key thermal parameters and evaluate the materials' performance under varying thermal loads. Such approaches demonstrate the growing potential of infrared thermography not only as a diagnostic imaging technique but also as a robust tool for extracting thermal properties, a concept especially important for polymeric or composite systems characterized by low thermal conductivity and complex thermal behavior.

To move beyond surface observations and fully harness the capabilities of infrared thermography for material characterization, it becomes necessary to apply inverse analysis techniques. These techniques allow for the estimation of unknown thermal quantities, such as thermal conductivity, heat transfer coefficients, among other properties and parameters, directly from measured temperature fields. By solving inverse heat transfer problems, researchers can uncover information that would otherwise be difficult to access through direct measurements, especially in materials where the thermal response is often sensitive to small variations in properties. Even without the use of infrared imaging, inverse analysis has been widely explored in the literature to determine unknown parameters in complex thermal systems. For instance, Knupp [9] introduced an integral transform technique for the direct identification of thermal conductivity and thermal capacity in heterogeneous media. This method allowed for the simultaneous estimation of spatially variable thermal properties, enhancing the accuracy of thermal analyses in materials with non-uniform characteristics. Similarly, Naveira-Cotta et al. [10] utilized integral transformed temperature fields to identify thermophysical properties in heterogeneous media. Their work highlighted the effectiveness of integral transforms in stabilizing inverse solutions and improving the reliability of property estimations in complex materials. In the context of thermal contact conductance, Asif et al. [11] employed a transient approach with inverse heat conduction problems to estimate thermal contact conductance between metallic contacts. Their findings indicated that the transient inverse method provided accurate estimations with shorter experimental durations compared to steady-state approaches, making it advantageous for practical applications. Chen et al. [12] focused on estimating space-dependent thermal conductivity in functionally graded hollow cylinders by developing an inverse analysis framework; this approach successfully determined the spatial variation of thermal

conductivity, which is crucial for the design and analysis of advanced composite materials. Moreover, Mohebbi et al. [13] addressed the determination of space-dependent heat flux in heat conduction problems with variable thermal conductivity; their study presented an efficient inverse analysis method that accurately estimated heat flux distributions, even in the presence of complex thermal conductivity variations, thereby enhancing the understanding of heat transfer in non-homogeneous materials.

Another notable example of application of inverse methods was provided by Pacheco et al. [14], who proposed a real-time inverse analysis method for identifying high-magnitude boundary heat fluxes applied to flat plates. Their approach relied on the forward solution of the two-dimensional heat conduction problem, combined with regularization techniques to stabilize the estimation process. The study demonstrated the feasibility of accurately recovering large transient boundary fluxes using limited and noisy surface simulated temperature data. Instead of relying solely on infrared imaging, inverse analysis techniques have been widely implemented in conjunction with various types of experimental data. In particular, the combination of inverse methods with experimental velocimetry has proven effective in addressing problems in fluid mechanics. Pinheiro et al. [15] employed micro-Particle Image Velocimetry (micro-PIV) measurements to estimate irregular microchannel geometries by applying an integral transform-based inverse framework. Their study demonstrated that detailed flow field data, when coupled with inverse analysis, enables accurate reconstruction of complex geometrical features that are otherwise challenging to characterize. Collectively, these studies underscore the versatility and effectiveness of inverse analysis techniques in extracting critical parameters across various complex systems.

Integrating inverse methods with infrared thermography has significantly expanded the possibilities for quantitative thermal characterization, particularly in cases where direct measurement is impractical. One early example of this integration is the work of Sousa et al. [16], who demonstrated how thermographic measurements could be effectively used as boundary conditions for solving three-dimensional inverse heat flux problems, leading to improvements in both spatial resolution and estimation reliability. Following this direction, research efforts have evolved toward increasingly sophisticated formulations that combine infrared measurements with inverse problem strategies to characterize not only boundary fluxes but also internal material properties and thermal behavior. The application of infrared-based inverse techniques has been extended to the detection of internal defects, as shown by Liu et al. [17], who addressed delamination defects in multilayered structures through a Fourier series-based inversion scheme. This reflects a broader trend in the literature toward extracting detailed internal information from surface temperature fields, a challenge also tackled in electronics, where Egger et al. [18] used Kalman filtering to estimate spatially varying heat sources in microprocessor hotspots, highlighting the potential for real-time thermal monitoring.

Other works have emphasized refining the estimation of heat transfer coefficients and heat flux distributions from infrared data. For example, Bozzoli et al. [19] applied inverse analysis to evaluate convective heat transfer in displaced enhancement devices, while Sanches et al. [20] focused on overcoming the ill-posed nature of explicit heat flux estimation by employing regularization techniques based on eigenfunction truncations. These studies demonstrate how stabilization methods and careful mathematical formulation are critical when recovering physical parameters from thermal images. At the material characterization level, infrared thermography has been combined with inverse methods to determine thermal properties directly. Chudzik [21,22] explored the estimation of thermal parameters such as conductivity and diffusivity in insulating materials, showing how non-invasive infrared measurements can provide quantitative results comparable to traditional intrusive methods. Similarly, Mohebbi and Sellier [23] applied a two-dimensional inverse analysis to irregular bodies, confirming the feasibility of using infrared-assisted inverse approaches for complex geometries. Several studies have also addressed the estimation of dynamic or time-varying thermal behaviors. Le Niliot and Gallet [24] and Huang and Fang [25] investigated methods for recovering transient boundary conditions and dynamic surface heat fluxes using infrared measurements, while Bauzin et al. [26] extended the concept to 3D transient heat source identification. This shift toward transient analysis reflects a growing interest in capturing not only steady-state properties but also temporal evolutions in thermal systems. Finally, advances have been made in the simultaneous estimation of multiple thermal properties, particularly in anisotropic or heterogeneous materials. Somasundharam and Reddy [27] addressed orthotropic materials, integrating infrared measurements to estimate directional conductivities, whereas Helmig et al. [28] developed experimental methods to quantify multi-scale thermal resistances at non-conforming interfaces, essential for the thermal management of layered composites. Millan [29], in turn, proposed a parameter reduction strategy for sequentially solving complex three-dimensional unsteady inverse problems with infrared thermography data, further pushing the computational efficiency in this field. These developments reveal a progression from simple flux estimation to advanced property recovery, supporting the present study's use of inverse methods to estimate the Biot number in polymeric materials.

As evidenced by the cornucopia of reviewed studies, the integration of infrared thermography with inverse analysis techniques for estimating thermal properties is well established in the literature. Traditional inverse methods have demonstrated considerable success in recovering heat fluxes, boundary conditions, and material parameters across a wide range of applications. However, despite the maturity of these approaches, there remains a notable scarcity of investigations exploring alternative methodologies, particularly those based on Machine Learning techniques. Classical inverse formulations typically rely on explicit mathematical models and regularization strategies to mitigate the ill-posedness of the problem. In contrast, Machine Learning offers a flexible, data-driven framework capable of capturing thermal behaviors and inferring parameters even under high measurement noise, conditions which are often encountered in polymeric materials. Recent studies have begun to highlight this potential: Zhu et al. [30] demonstrated that deep learning methods can effectively estimate boundary condition parameters in transient heat transfer problems, while Sarhadi et al. [31] applied Machine Learning to thermal imaging for damage detection in glass–epoxy composites. Nevertheless, few studies have systematically explored the generation of synthetic thermal datasets from forward thermal problems to train Machine Learning models for quantitative parameter estimation, nor have they rigorously compared the performance of these data-driven approaches with classical inverse methods under different boundary conditions. This is a gap that Physics-Informed Machine Learning (PIML) have recently begun to address. By embedding physical laws, such as governing partial differential equations, directly into the training process, Physics-Informed methods combine the predictive flexibility of neural networks with the rigor of classical formulations, allowing for more robust parameter estimation even with sparse or noisy measurements. Recent works have applied Physics-Informed Neural Networks (PINNs) to estimate thermal conductivity in practical scenarios, including battery thermal modeling, as shown in studies investigated by Jo et al. [32]. Moreover, Cai et al. [33] provided a detailed review for heat transfer problems, demonstrating the application of PINNs to canonical heat conduction problems and validating their effectiveness in reconstructing temperature fields and material properties. Although promising, these methodologies are still relatively recent, and comprehensive comparisons with traditional inverse techniques under varying experimental and boundary condition complexities remain a rich area for future research.

The purpose of this work is to introduce an investigation into two-dimensional heat conduction in polymeric materials and the estimation of thermal properties using inverse analysis and machine learning

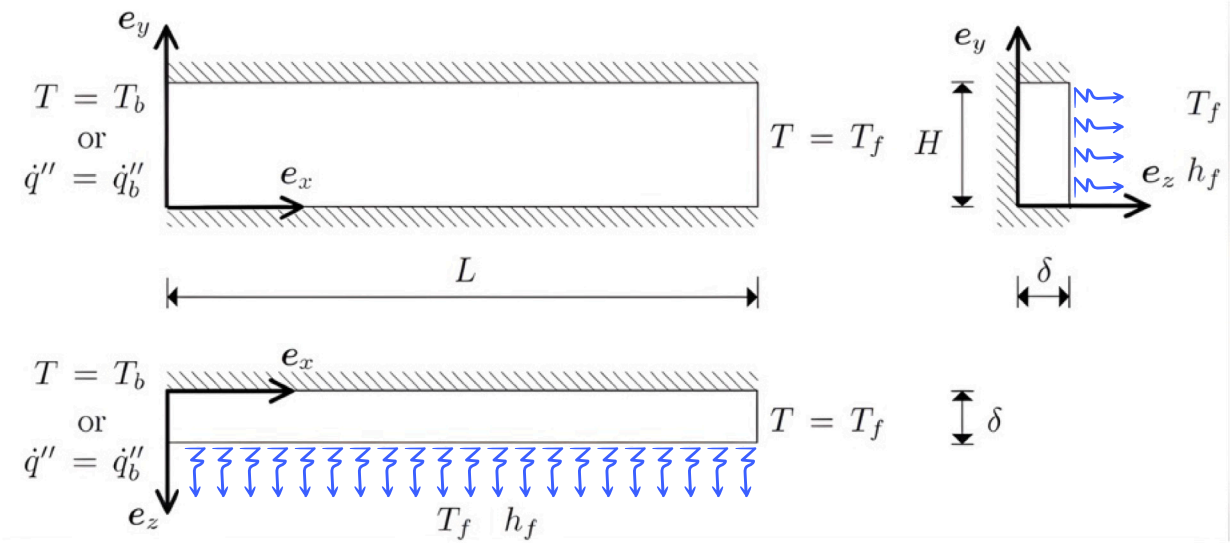

Fig. 1. Schematic diagram of the considered problem, addapted from Moreira et al. [45].

techniques. Building upon the extensive literature on infrared thermography and inverse problems, this study advances toward a more systematic integration of classical modeling and data-driven approaches for characterizing thermophysical parameters. The experimental data used in this work was obtained from the setup developed by Moreira et al. [34], who also proposed a simplified one-dimensional lumped-parameter analytical model using infrared thermography to estimate the thermal conductivity of epoxy nanocomposites. While their approach provided valuable insights into thermal conductivity trends, it did not address the estimation of dimensionless parameters such as the Biot number, nor did it incorporate regularization strategies to stabilize the inverse solution. Unlike Moreira et al. [34], the present investigation focuses on estimating the Biot number in polymeric materials by employing a reduced-order thermal model with enhanced sensitivity to boundary conditions. In addition, rather than relying on a simple one-dimensional model, a full two-dimensional formulation is employed. The model is solved using the integral transform technique, building upon previous applications of this methodology [35–44]. The forward solution of the 2D model is used to generate synthetic thermal data for training and evaluation purposes. Unlike prior studies, which predominantly relied on inverse analysis methods alone, this work systematically compares the classical and regularized Levenberg–Marquardt-based inverse solution with a supervised machine learning model trained on synthetic datasets. Moreover, two different base boundary conditions — Dirichlet and Neumann — are investigated to evaluate the sensitivity of parameter estimation strategies. All simulations, dataset generation, and training procedures are implemented within the *Wolfram Mathematica*® environment, ensuring consistency and methodological integration. This combined analytical, numerical, and data-driven framework provides a comprehensive approach for the thermal characterization of polymeric systems using infrared thermography.

2. Problem statement

2.1. Forward problem

The problem herein considered is that of steady heat conduction in a rectangular cross-section fin: a prismatic body with a heat source applied at one face. The other faces are thermally insulated or exchange heat with the environment, as depicted in Fig. 1.

As can be seen, the base of the fin is positioned at $x = 0$ and two heating models are considered: the first is characterized by a Dirichlet boundary condition, whereas the second involves a Neumann boundary condition. Also, a long-fin model is considered such that the fin tip ($x = L$) is in equilibrium with the environment temperature, T_f. The steady regime is achieved with all heat input at the base being lost to the environment at the surface $z = \delta$, where a Robin boundary condition is applied to represent this configuration. Naturally, this implies that the remaining surfaces are surfaces ($y = 0$, $y = H$ and $z = 0$) are thermally insulated. The heat transfer coefficient at the surface $z = \delta$ is allowed to vary with the axial coordinate only, such that a two-dimensional formulation can be employed.

According to the previous description, the heat transfer problem is governed by the following equations:

$$\frac{\partial^2 T}{\partial x^2} + \frac{\partial^2 T}{\partial z^2} = 0 \quad \text{in} \quad 0 < x < L \quad \text{and} \quad 0 < z < \delta, \tag{1a}$$

$$-k\frac{\partial T}{\partial x} = \varphi(T - T_b) + \dot{q}''_b \quad \text{at} \quad x = 0, \quad \text{for} \quad 0 < z < \delta, \tag{1b}$$

$$T = T_f \quad \text{at} \quad x = L, \quad \text{for} \quad 0 < z < \delta, \tag{1c}$$

$$\frac{\partial T}{\partial z} = 0 \quad \text{at} \quad z = 0, \quad \text{for} \quad 0 < x < L, \tag{1d}$$

$$k\frac{\partial T}{\partial z} + h_f(T - T_f) = 0 \quad \text{at} \quad z = \delta, \quad \text{for} \quad 0 < x < L, \tag{1e}$$

where T is the temperature, x and z are the spatial coordinates, k is the thermal conductivity, h_f is the convective heat transfer coefficient, $\dot{q}''_b$ is the heat flux at the base of the fin, φ is a generalized boundary condition parameter, L is the length of the fin and δ is the thickness of the fin. A general boundary condition at the base is used, where $\varphi \to \infty$ gives a uniform base temperature (Dirichlet condition) while $\varphi = 0$ yields a uniform flux (Neumann condition) at the base.

In order to facilitate the inverse analysis, a normalized version of the problem is employed. The normalization process is carried out by introducing the following dimensionless quantities:

$$\xi = \frac{x}{L}, \qquad \zeta = \frac{z}{\delta}, \qquad \theta = \frac{T - T_f}{\Delta T}, \tag{2a-c}$$

where $\Delta T = T_b - T_f$, with T_b representing the base temperature and T_f denoting the ambient air temperature surrounding the fin. In cases where a heat flux is imposed at the base, T_b is not explicitly prescribed; rather, it emerges as part of the solution and is not known a priori. Naturally, in these cases, T_b depends on the imposed heat flux $\dot{q}''_b$; however, rather than using the traditional definition $\Delta T = (L/k)\,\dot{q}''_b$, T_b

is retained as a separate parameter to enable direct comparison with the Dirichlet base boundary condition case.

The dimensionless mathematical formulation for the two-dimensional steady heat conduction problem can be rewritten as:

$$\frac{\partial^2\theta}{\partial\xi^2} + \frac{1}{\gamma^2}\frac{\partial^2\theta}{\partial\zeta^2} = 0 \quad \text{in} \quad 0 < \xi < 1 \quad \text{and} \quad 0 < \zeta < 1, \tag{3a}$$

$$-\frac{\partial\theta}{\partial\xi} = \varphi^*(\theta - 1) + q^*, \quad \text{at} \quad \xi = 0, \quad \text{for} \quad 0 < \zeta < 1, \tag{3b}$$

$$\theta = 0 \quad \text{in} \quad \xi = 1, \quad \text{for} \quad 0 < \zeta < 1, \tag{3c}$$

$$\frac{\partial\theta}{\partial\zeta} = 0 \quad \text{in} \quad \zeta = 0, \quad \text{for} \quad 0 < \xi < 1, \tag{3d}$$

$$\frac{\partial\theta}{\partial\zeta} + \mathrm{Bi}\,\theta = 0 \quad \text{in} \quad \zeta = 1, \quad \text{for} \quad 0 < \xi < 1, \tag{3e}$$

where θ is the dimensionless temperature, while ξ and ζ are the dimensionless spatial variables. As previously outlined, an important dimensionless parameter is obtained in the dimensionless problem, the Biot Number (Bi). Also other dimensionless quantities are obtained, such as the aspect ratio of the bar γ and the dimensionless heat flux q^* of the base, respectively:

$$\mathrm{Bi} = \frac{h_f\,\delta}{k}, \qquad \varphi^* = \frac{\varphi\,L}{k}, \qquad \gamma = \frac{\delta}{L}, \qquad q^* = \frac{L\,q_b''}{k\,\Delta T}, \tag{4a-c}$$

One can readily show that, for the Neumann boundary condition case, the dimensionless heat flux q^* is directly related to the average base temperature $\theta_{av,b}$, defined as

$$\theta_{av,b} = \int_0^1 \theta(0,\zeta)\,\mathrm{d}\zeta, \tag{5}$$

which is not known *a priori*. As previously discussed, to facilitate comparison with the Dirichlet case, the value of q^* is selected such that $\theta_{av,b} = 1$.

3. Integral transform solution

The direct analytical solution is calculated for both cases through the use of the Classical Integral Transform Technique (CITT), extensively revised by Mikhailov and Özisik [46]. The solution procedure requires the definition of the transformation pair, as follows:

$$\text{Transform} \quad \Longrightarrow \quad \overline{\theta}_n(\xi) = \int_0^1 \theta(\xi,\zeta)Z_n(\zeta)\,\mathrm{d}\zeta, \tag{6a}$$

$$\text{Inverse} \quad \Longrightarrow \quad \theta(\xi,\zeta) = \sum_{n=1}^{\infty}\frac{\overline{\theta}_n(\xi)\,Z_n(\zeta)}{N_n}, \tag{6b}$$

where Z_m are orthogonal functions stemming from the solution of a Sturm–Liouville problem, herein defined by the one-dimensional Helmholtz problem:

$$Z_n''(\zeta) + \mu_m^2\,Z_n(\zeta) = 0, \qquad \text{for} \qquad 0 \le \zeta \le 1, \tag{7a}$$

$$Z_n'(0) = 0, \qquad Z_n'(1) + \mathrm{Bi}\,Z_n(1) = 0, \tag{7b}$$

which admits the infinite nontrivial solutions in the form:

$$Z_n(\zeta) = \cos(\mu_n\,\zeta), \tag{8a}$$

where the eigenvalues are obtained from the solution of the transcendental equation:

$$\mu_n\,\sin(\mu_n) = \mathrm{Bi}\,\cos(\mu_n), \tag{8b}$$

in which n is a positive integer, and the norms N_n are calculated through:

$$N_n = \int_0^1 \cos^2(\mu_n\,\zeta)\,\mathrm{d}\zeta = \frac{\mu_n + \cos(\mu_n)\,\sin(\mu_n)}{2\,\mu_n}. \tag{8c}$$

The Integral Transform Technique procedure relies on the transformation of the given problem by multiplying Eq. (3a) by Z_n, integrating within $0 \le \zeta \le 1$:

$$\int_0^1 \frac{\partial^2\theta}{\partial\xi^2}\,Z_m\,\mathrm{d}\zeta + \frac{1}{\gamma^2}\int_0^1 \frac{\partial^2\theta}{\partial\zeta^2}\,Z_m\,\mathrm{d}\zeta = 0. \tag{9}$$

Because of the homogeneous boundary conditions in $0 \le \zeta \le 1$, the final transformed ODE is obtained:

$$\frac{\partial^2\overline{\theta}_n}{\partial\xi^2} - \frac{\mu_n^2}{\gamma^2}\,\overline{\theta}_n = 0. \tag{10}$$

The solution for the transformed potentials $\overline{\theta}_n$ is readily obtained as:

$$\overline{\theta}_n = A_n\,\sinh\left[\frac{\mu_n}{\gamma}\,(1-\xi)\right]. \tag{11}$$

This solution is applied to the inversion formula (6b) and an analytical solution for $\theta(\xi,\zeta)$ is finally obtained, valid for both Case 1 and Case 2:

$$\theta(\xi,\zeta) = \alpha\sum_{n=1}^{\infty}\frac{A_n}{N_n}\,\sinh\left[\frac{\mu_n}{\gamma}\,(1-\xi)\right]\cos(\mu_n\,\zeta). \tag{12}$$

The constants A_n and σ depend on the boundary condition at $\xi = 0$ and must be separately determined for each case. In Case 1, the parameter α parameter is equal to 1, and the coefficients A_n are calculated through the expression:

$$A_n = \frac{\sin(\mu_n\,\zeta)}{\mu_n}\,\mathrm{csch}\left(\frac{\mu_n}{\gamma}\right), \tag{13}$$

and there is no need to calculate q^*. Conversely, for Case 2, the direct analytical solution is obtained with A_n and q^* given by:

$$A_n = \frac{\sin(\mu_n\,\zeta)}{\mu_n}\,\frac{\gamma}{\mu_n}\,\mathrm{sech}\left(\frac{\mu_n}{\gamma}\right), \tag{14a}$$

$$\alpha = q^* = \left[\sum_{n=1}^{\infty}\frac{A_n}{\mu_n}\,\sin(\mu_n)\,\sinh\left(\frac{\mu_n}{\gamma}\right)\right]^{-1}. \tag{14b}$$

From the solution given by Eq. (12), the surface temperature distribution can be directly obtained as:

$$\varphi(\xi) = \theta(\xi,1) = \alpha\sum_{n=1}^{\infty}A_n\cos(\mu_n)\sinh\left(\mu_n\gamma^{-1}(1-\xi)\right), \tag{15}$$

4. Parameter estimation

4.1. Inverse analysis

For the estimation of the Biot Number, an inverse analysis is conducted with the application of the Levenberg–Marquardt Method for parameter estimation. This technique consists on an iterative method that tends to the Gauss–Newton method in the neighborhood of the minimum of the ordinary least squares norm. It was named after Levenberg [47], who first developed the technique in 1944, and Marquardt [48], who modified the method using a different approach.

First, the inverse analysis procedure requires the reformulation of an ill-posed problem into a well-posed approximation. There are different stabilization techniques to fulfill this requirement, such as the Tikhonov's Regularization [49], Alifanov's Iterative Regularization Methods [50,51] or Beck's Sequential Function Specification Technique [52,53]. In the present work, an in-house Levenberg–Marquardt algorithm was employed that incorporates diagonal-scaled damping and a reference-guided regularization scheme. A flowchart illustrating the complete inverse methodology is shown in Fig. 2.

Since this problem involves the estimation of a single parameter, the ordinary least squares norm is used as the objective function (S) to stabilize the inverse problem, as shown in the following equation:

$$S = (\mathbf{Y} - \mathbf{T})^T\,(\mathbf{Y} - \mathbf{T}). \tag{16}$$

Here, the residual vector, $\mathbf{R}$, is expressed as the difference between the measured temperature data, $\mathbf{Y}$, and the temperature predicted by the direct model, $\mathbf{T}$:

$$\mathbf{R} = \mathbf{Y} - \mathbf{T}. \tag{17}$$

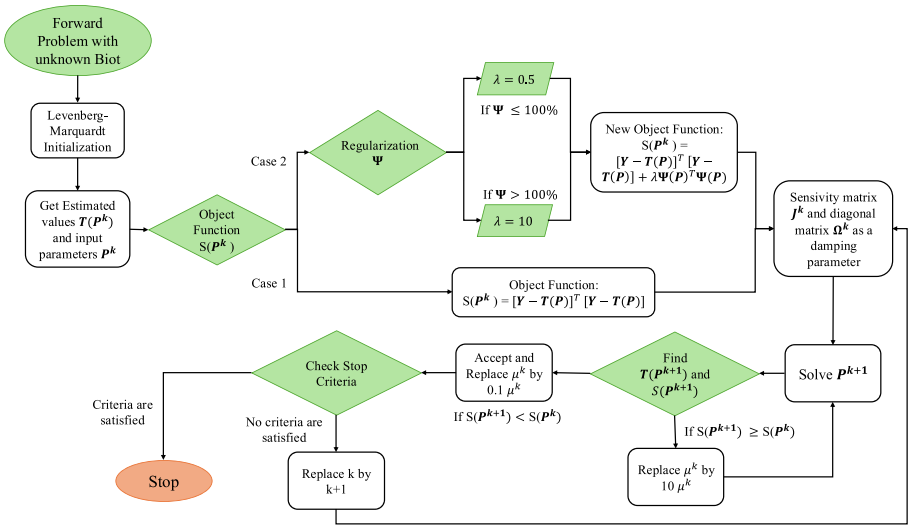

Fig. 2. In-house code flowchart for Biot number estimation using Levenberg–Marquardt (LM) with a scaled damping and reference regularization.

This residual vector quantifies the mismatch between model and data and is fundamental in both the gradient and update steps of the Levenberg–Marquardt algorithm.

Following the steps outlined by Özışık and Orlande [54], the algorithm begins with a sensitivity analysis. The sensitivity coefficients (J_{ij}) provide insight into the relationship between the model output and the estimated parameters, and can guide experimental design and improve inversion robustness. In this work, the sensitivity matrix is calculated using finite-difference approximations, as expressed in the following equation:

$$J_{ij} = \frac{T_i(P_1, P_2, \ldots, P_j + \epsilon\, P_j, \ldots, P_{max}) - T_i(P_1, P_2, \ldots, P_j, \ldots, P_{max})}{\epsilon\, P_j}, \quad (18)$$

in which P_j refers to the parameter being perturbed, and ϵ is a small perturbation factor. The index i refers to the spatial or measurement location of the temperature field, whereas the index j corresponds to the parameter under estimation (the Biot number).

As previously noted, sensitivity analysis reveals important information about the problem. A more specific criterion for assessing the influence of the sensitivity matrix on the stability of the inverse problem is the identifiability condition, defined by:

$$\left|\mathbf{J}^T\,\mathbf{J}\right| \neq 0. \quad (19)$$

Small values of the determinant $|\mathbf{J}^T\,\mathbf{J}|$ may indicate difficulties in the implementation of the iterative procedure due to near-linearly dependent columns in the sensitivity matrix, which can amplify numerical instabilities. While the Jacobian product $|\mathbf{J}^T\,\mathbf{J}|$ may not be as critical in problems governed by Dirichlet boundary conditions where the temperature values are directly prescribed, it becomes significantly more influential in the case of Neumann boundary conditions. Under Neumann conditions at the base of the fin, the boundary input is a heat flux rather than a fixed temperature, which often leads to a flatter or less sensitive temperature distribution in the domain. As a result, the corresponding columns of the sensitivity matrix (Jacobian) can become nearly linearly dependent, making $|\mathbf{J}^T\,\mathbf{J}|$ poorly conditioned and prone to numerical instability. In order to mitigate this effect, a diagonal-scaled damping term is applied to the Jacobian product with a scaled diagonal form $\mu_k\, diag(\mathbf{J}^T\,\mathbf{J})$, enhancing numerical stability while respecting parameter scaling.

To further stabilize the solution and guide the inverse process, a reference-guided regularization term is introduced to softly constrain parameter estimates around a nominal or expected value. This penalty term is activated adaptively: if the relative deviation between the current parameter estimate and the reference value exceeds a threshold (e.g., greater than 100%), the regularization weight λ is dynamically adjusted based on this deviation. Specifically, when the estimated parameter deviates by more than 100% from the reference, a strong penalty ($\lambda = 10$) is applied to suppress divergence and reinforce solution stability. Conversely, when the parameter remains within an acceptable range (less than or equal to 100% deviation), a milder penalty ($\lambda = 0.5$) is used, maintaining flexibility in the estimation while still providing numerical damping. This adaptive weighting strategy is particularly well-suited to Biot number estimation, where the parameter directly affects thermal boundary conditions and typically varies within a limited physical range. Excessive deviations may yield nonphysical interpretations of heat transfer behavior; thus, the selected λ values serve to constrain the solution within thermally meaningful bounds, especially in ill-posed scenarios or when model sensitivity to the Biot number is low.

The modified parameter updating equation thus becomes:

$$\Delta\mathbf{P}_k = \left(\mathbf{J}^T\mathbf{J} + \mu_k\,\Omega_k\right)^{-1}\mathbf{J}^T\,(\mathbf{Y} - \mathbf{T}), \quad (20)$$

where $\Omega_k = \mathrm{diag}(\mathbf{J}^T\mathbf{J})$. Additionally, the cost function is augmented to include the reference-guided regularization term:

$$S = (\mathbf{Y} - \mathbf{T})^T\,(\mathbf{Y} - \mathbf{T}) + \lambda\,\mathbf{\Psi}^T\,\mathbf{\Psi} \quad (21)$$

where,

$$\mathbf{\Psi}(\mathbf{P}) = \frac{\mathbf{P} - P_{ref}}{P_{ref}} \quad (22)$$

The full Levenberg–Marquardt code was designed to accommodate flexible inputs from analytical–numerical models and enables real-time monitoring of convergence. To improve numerical stability, especially during the early iterations or when the residual norm is large, a stabilizing strategy is adopted by defining the regularization parameter as $\mu_k = 0.01\,\|\mathbf{Y}\|$. This choice ensures that the damping parameter scales appropriately with the magnitude of the experimental or simulated data, preventing divergence due to ill-conditioning of the Jacobian matrix, in line with scaling-based heuristics commonly adopted in nonlinear inverse problems and inverse heat transfer analysis [52,54]. In addition, the reference parameter P_{ref} used in the regularization term is taken equal to the initial guess of the estimated parameter, acting as a numerical scaling reference without biasing the solution. This algorithm was implemented using the *Wolfram Mathematica*® platform [55].

4.2. Machine learning

In this work, a supervised Machine Learning method is also applied to estimate the Biot number from infrared thermographic data

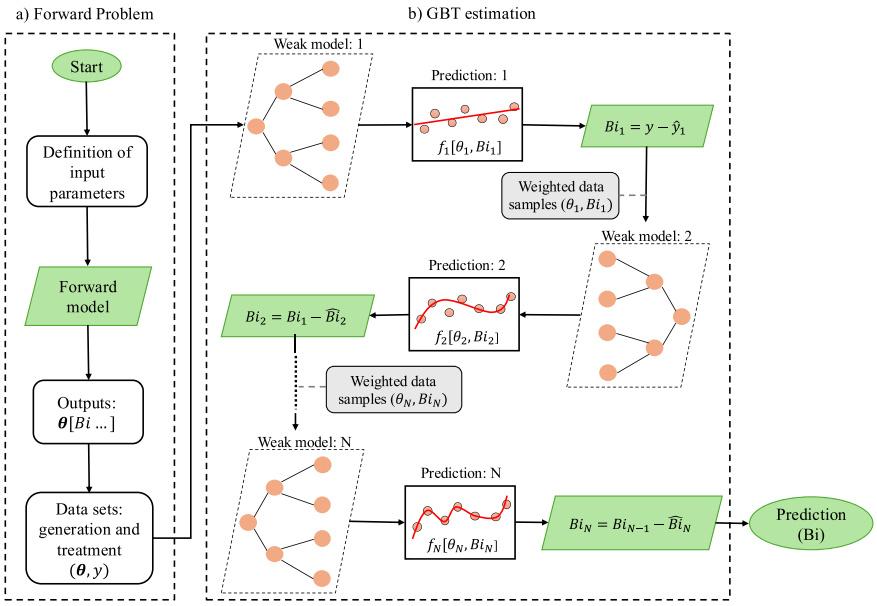

Fig. 3. Schematic of Biot number estimation using Gradient Boosted Trees (GBT). (a) Forward problem setup with synthetic data generation. (b) GBT architecture illustrating successive predictions from weak learners and weighted samples.

of polymeric fins. The Machine Learning model is trained to perform regression, not classification, since the objective is to predict a quantity (the Biot number), which reflects the ratio of convective to conductive heat transfer at the surface of the material.

The training data for the Machine Learning model are not based on direct experimental measurements but instead on synthetic data generated by solving a dimensionless two-dimensional steady-state heat conduction problem using Biot numbers ranging from 0.001 to 20. For different Biot numbers, synthetic temperature fields are generated at the surface of the fin (at $z = 1$). Each generated temperature distribution is a spatially correlated input, reflecting how temperature varies smoothly across the fin under steady-state conditions.

Additionally, because experimental datasets will not be extremely large, but rather moderate in size, the selected Machine Learning approach must perform well under small-to-medium dataset conditions. Therefore, the Gradient Boosted Trees (GBT) methodology is selected. This technique builds a strong prediction model by sequentially adding decision trees, each one trying to correct the errors made by the previous one, resulting in a robust and highly accurate regressor even when the data is noisy or limited in volume. Fig. 3 illustrates the flowchart for Biot number prediction using Gradient Boosted Trees (GBT). On the left (a), the forward problem involves defining input parameters and computing the corresponding dimensionless temperature field θ through a forward model, generating datasets. Before inputting this dataset into the GBT model, the data is randomized using the *Mathematica* function **RandomSample** to avoid bias in model training due to any ordering in the dataset. On the right (b), the GBT estimation proceeds iteratively by training a sequence of weak learners. The first model provides an initial Biot number prediction, after which the residual error is computed and used as the target for the next learner. At each iteration, the training samples are re-weighted to emphasize regions associated with larger residuals, allowing subsequent models to focus on correcting the remaining error. The final Biot number prediction is obtained by combining the contributions of all weak learners, yielding a robust estimator even for noisy or moderately sized datasets.

Mathematically, the training process is framed as minimizing a Mean Squared Error (MSE) loss function:

$$\mathrm{MSE} = \frac{1}{N}\sum_{i=1}^{N}\left(y_i - \hat{f}(\boldsymbol{\Theta}_i)\right) \tag{23}$$

where N is the number of synthetic samples, $\boldsymbol{\Theta}_i$ is the ith temperature profile input, and y_i is the corresponding true Biot number.

The prediction model $\hat{f}$ is built incrementally, with the following update rule at iteration m:

$$\hat{f}_m(\boldsymbol{\Theta}) = \hat{f}_{m-1}(\boldsymbol{\Theta}) + \nu\, h_m(\boldsymbol{\Theta}) \tag{24}$$

where h_m is the new weak learner fitted to the residuals of the previous model, and ν is the learning rate controlling the contribution of each learner to the ensemble.

Once trained, the final prediction for a new experimental temperature profile $\boldsymbol{\Theta}_{exp}$ capture by the infrared camera is given by:

$$\hat{y} = \hat{f}(\boldsymbol{\Theta}_{exp}) \tag{25}$$

Thus, this ML strategy provides a flexible and noise-resilient method for estimating the Biot number, complementing classical inverse problem solutions while potentially offering greater robustness. As already stated the computational process will be implemented using *Wolfram Mathematica*® [55]. In particular, the training of the Gradient Boosted Trees model is performed using the **Predict** routine with the method "GradientBoostedTrees". The main hyperparameters, including the learning rate, maximum number of training rounds, and maximum tree depth, are automatically selected by the internal optimization procedure of Mathematica according to the specified performance goal. For the present study, the resulting configuration corresponds to a learning rate of 0.2, a maximum of 50 training rounds, and a maximum tree depth of 6, with a minimum leaf size of 200. Model validation is further enhanced using the "CrossValidationReport" option to assess generalization performance and robustness. Once trained, the resulting "PredictorFunction" is employed to estimate the Biot number from new infrared thermographic data.

5. Experimental setup

In order to acquire the experimental temperature data, the IR thermography apparatus is prepared with an initial elaboration of a supporting structure to hold the samples. The complete experimental setup can be visualized in Fig. 4. The adaptation of the experimental procedure aimed to replicate as closely as possible the assumptions made in the mathematical modeling. To maintain a uniform and constant temperature at the bar base ($x = 0$), a Peltier plate was employed.

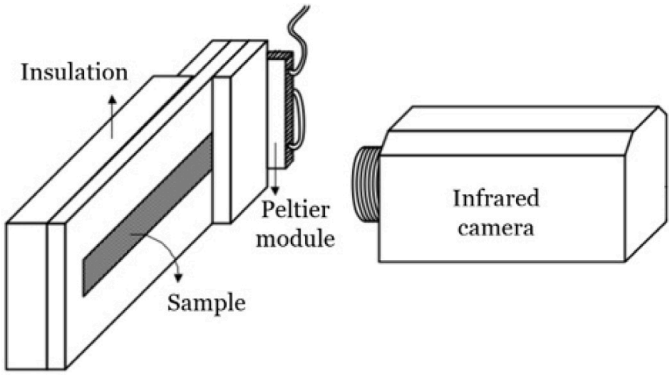

Fig. 4. Experimental setup.

Table 1
Specifications for the IR camera Flir A325G.

Vision Field/minimum distance from the object (Built in)	25° × 18.8°/0.4 m
Vision Field/minimum distance from the object (with lens)	45° × 33.8°/0.2 m
Type of detector	Microbolometer
Spectrum Range	7.5 – 13 μm
Resolution	320 × 240 pixels
Temperature measurement range	0 – 350 °C
Sensibility	< 0.07 °C to 30 °C
Precision (in percentage of reading)	± 2 °C or ± 2 %
Maximum frequency of imaging capture	9 Hz

Additionally, to enhance thermal contact and minimize interface resistance, a thin layer of silicon-based thermal paste was applied between the Peltier plate and the base of the sample. According to the theoretical assumptions, the surfaces at $z = 0$, $y = 0$, and $y = b$ were thermally insulated, while the frontal surface was coated with black paint — providing near-unity surface emissivity — and exposed to natural convective heat transfer with the surrounding air at ambient temperature.

The infrared camera model used in the experiments was the Flir A325G, equipped with a 9.7 mm focal length lens. Temperature field acquisition was performed using the Flir Thermacam Researcher 2.9 Pro software. The main specifications of the infrared camera are summarized in 1.

All experimental tests were conducted under stationary regime conditions to ensure steady-state heat transfer throughout the fin during data acquisition. Fig. 5 shows one of the infrared images of the sample superimposed with a visible image for reference. The surface temperature distribution measured under steady-state reveals a thermal gradient along the bar length, with temperatures ranging approximately from 38.4°C at the base to 25.1°C at the tip. Notably, the temperature variation along the y-axis appeared negligible, validating the two-dimensional model assumptions. Furthermore, it was observed that nearly one-third of the bar length stabilized close to 25.1°C, corroborating the use of prescribed temperature boundary conditions at the tip and confirming the validity of the experimental setup for the intended modeling analysis.

6. Results and discussion

This section presents the numerical results obtained by the direct mathematical formulation described in this work, the experimental data from 5 tests performed through the Infrared Thermography camera and the parameter estimation conducted by both Levenberg–Marquardt Method and the Gradient Boosted Trees. A preliminary analysis of the experimental data is presented, so as all the graphics and values of the temperature field can be seen. The direct problem is solved for two boundary conditions at the base of the fin: Case 1

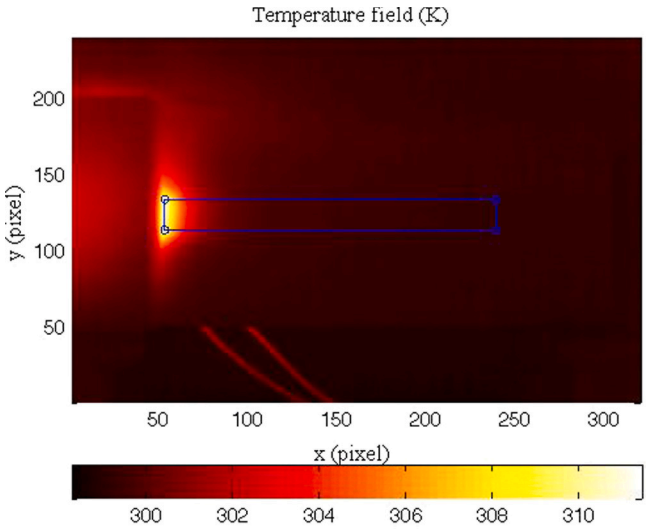

Fig. 5. Experimental Temperature field.

corresponds to a Dirichlet condition (prescribed temperature), while Case 2 to a Neumann condition (prescribed heat flux).

6.1. Experimental data and input parameters

The thermal characterization was performed on an acrylic sample with thermal conductivity of $0.179 \pm 0.003\,\mathrm{W/(m\,K)}$, according to the data obtained by the Heat Flow Meter Instrument FOX 50. While the Heat Flow meter measurements were conducted to determine the thermal conductivity, the IR experiments were conducted to estimate the rest of the thermal parameters through Biot number analysis.

Five independent tests were carried out under stationary regime conditions using the infrared thermography setup described previously. The surface temperature fields were captured by the infrared camera, and the first set of results is presented in Fig. 5, illustrating the typical thermal behavior along the fin surface.

The physical dimensions of the tested sample correspond to those used in the direct mathematical model formulation. The rectangular fin presents a length of $L = 100.36\,\mathrm{mm}$, a width of $H = 12.62\,\mathrm{mm}$, and a thickness of $\delta = 4.84\,\mathrm{mm}$. From these dimensions, the aspect ratio can be calculated as:

$$\gamma = \frac{\delta}{L} = 0.04823 \approx 0.05 \tag{26}$$

This two-dimensional configuration ensures that the conduction along the longitudinal (x) and thickness (z) directions is properly captured, while conduction along the width (y) direction can be considered negligible, as corroborated by the primary experimental observations.

A summary of the main input parameters used in both the experimental measurements and direct numerical calculations is presented in Table 2. It is important to note that the surface was coated with black paint to ensure high and uniform infrared emissivity, and the value of approximately 0.95, provided by the infrared camera, was obtained.

For each test, the temperature distribution was acquired along different positions in the dimensionless longitudinal coordinate ξ. Fig. 6 shows the experimental temperature distribution along the acrylic sample, with T_{exp} plotted against x (mm). The individual curves in Fig. 6a correspond to five independent tests, illustrating the reproducibility and variability of the measurements. Fig. 6b presents the fitted temperature profile obtained from these data together with the associated error bars, which provide a quantitative measure of experimental uncertainty along the sample length.

As can be observed, the temperature consistently decreases along the longitudinal direction (ξ), following the expected heat dissipation

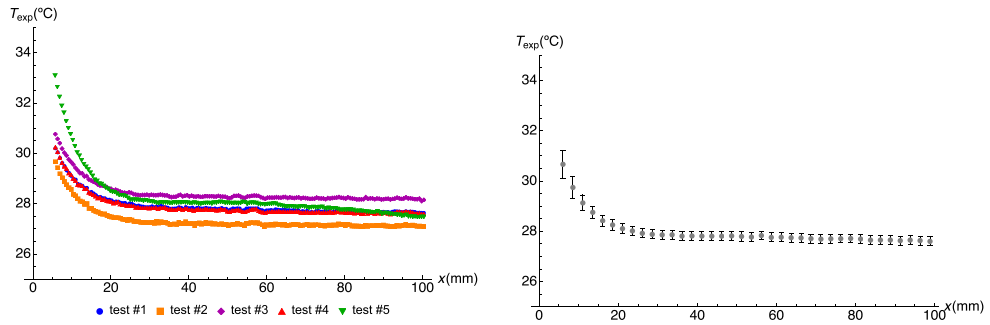

(a) Experimental temperature points for 5 tests (b) Fitted temperature data and Error Bar

Fig. 6. Temperature distribution measured along the acrylic sample for five independent experimental tests. Each curve represents a different test, showing the variability of the measured temperatures as a function of the position x (mm).

Table 2
Summary of input parameters for the experimental setup and mathematical modeling.

Parameter	Value
Sample material	Acrylic
Thermal conductivity, k	0.17866 W/(m K)
Sample length, L	100.36 mm
Sample width, H	12.62 mm
Sample thickness, δ	4.84 mm
Aspect ratio, γ	0.05
Emissivity (painted surface), ϵ	≈ 0.95
Ambient temperature, T_f	25 °C

trend from the heated base toward the cooler tip of the fin. Fig. 6 illustrates the measured temperature profiles obtained in the five experimental tests. The good agreement among the profiles indicates the reproducibility of the experimental procedure and provides a reliable basis for subsequent parameter estimation using inverse and Machine Learning techniques.

6.2. Preliminary training data analysis

In order to enable the application of inverse analysis and machine learning techniques for the estimation of thermal parameters, synthetic datasets were generated based on the forward solution of the two-dimensional steady-state heat conduction problem described previously.

The synthetic data were created by solving the dimensionless two-dimensional heat conduction equations using the Integral Transform Technique. For different prescribed Biot numbers, ranging from 0.001 to 20 (separated by 0.01), the surface temperature distributions $\theta(\xi, \zeta = 1)$ were computed. The aspect ratio γ was set according to the physical dimensions of the experimental sample ($\gamma \approx 0.05$), and convergence analyses were performed to guarantee the accuracy of the temperature fields. In all cases, a convergence criterion of 10^{-6} was adopted for the truncation of the infinite series solutions, ensuring the precision of the synthetic profiles.

Each synthetic data sample corresponds to a specific Biot number and its associated dimensionless surface temperature profile along the fin length (ξ direction). To mimic the infrared thermography measurements, only the temperatures at the surface $\zeta = 1$ were extracted, replicating the experimental conditions where the infrared camera captures the outer surface of the polymeric fin. These temperature profiles, discretized along ξ, were then stored along with their corresponding Biot number labels, forming the complete dataset used for training and testing the supervised machine learning model. Prior to the training process, the forward model predictions were compared against the experimental temperature profiles. This comparison was performed by normalizing the temperature data and calculating the mean squared error between the predicted and experimental profiles along the fin surface.

The Gradient Boosted Trees (GBT) model was trained using three randomized subsets of the synthetic dataset, containing 200, 1000, and 2000 samples, respectively. Randomization was employed to eliminate ordering bias during training and to promote model generalization across the full spectrum of thermal behaviors. Fig. 7 presents the learning curves based on Mean Absolute Error (MAE) analysis for Biot number estimation under Dirichlet (Case 1) and Neumann (Case 2) base conditions. The MAE is showed for training and test sets versus training data percentage. As can be seen, as the sample size increases from 200 to 2000, a noticeable reduction in MAE is observed for both cases, reflecting improved prediction accuracy and greater consistency. The curves tend to stabilize as the proportion of training data increases, indicating that beyond a certain point, the inclusion of additional data yields some improvements. For the Dirichlet boundary condition (Case 1), the training and test errors remain closely aligned across all sample sizes, suggesting good generalization and low susceptibility to overfitting. In contrast, the Neumann boundary condition (Case 2) presents slightly higher test errors compared to training errors, especially with smaller datasets, indicating greater sensitivity to measurement noise and higher uncertainty in parameter estimation based on surface heat flux information, which is seen also in the Levenberg–Marquardt analysis. Nonetheless, in both cases, the methodology shows satisfactory performance, with reduced error dispersion as the dataset size increases.

To ensure independent validation, a separate synthetic dataset — generated using the same forward model but excluded from the training phase — was reserved to assess the accuracy of both the inverse method and the machine learning approach. This test set simulates unseen experimental scenarios and is specifically designed to evaluate the robustness of the predictive strategy, particularly in estimating the Biot number. To further mimic real experimental conditions, an additional synthetic dataset was created by perturbing the exact temperature distribution $\mathbf{Y}$ with Gaussian noise. This noise, modeled as a standard normal variable ω, was scaled by 10% of the maximum temperature value across all 100 spatial points, yielding the noisy measurement data. These perturbed measurements simulate the variability typically observed in infrared thermography and are used specifically to test the inverse estimation process using the Levenberg–Marquardt algorithm. The combination of clean and noisy synthetic data enables rigorous validation of both deterministic and machine learning-based estimation frameworks under controlled and realistic conditions.

Finally, it is important to note that the synthetic training dataset is independent of the simulated data used in the subsequent evaluation steps. Moreover, the same synthetic dataset was employed to predict different Biot number values, highlighting the model's adaptability across varying thermal scenarios.

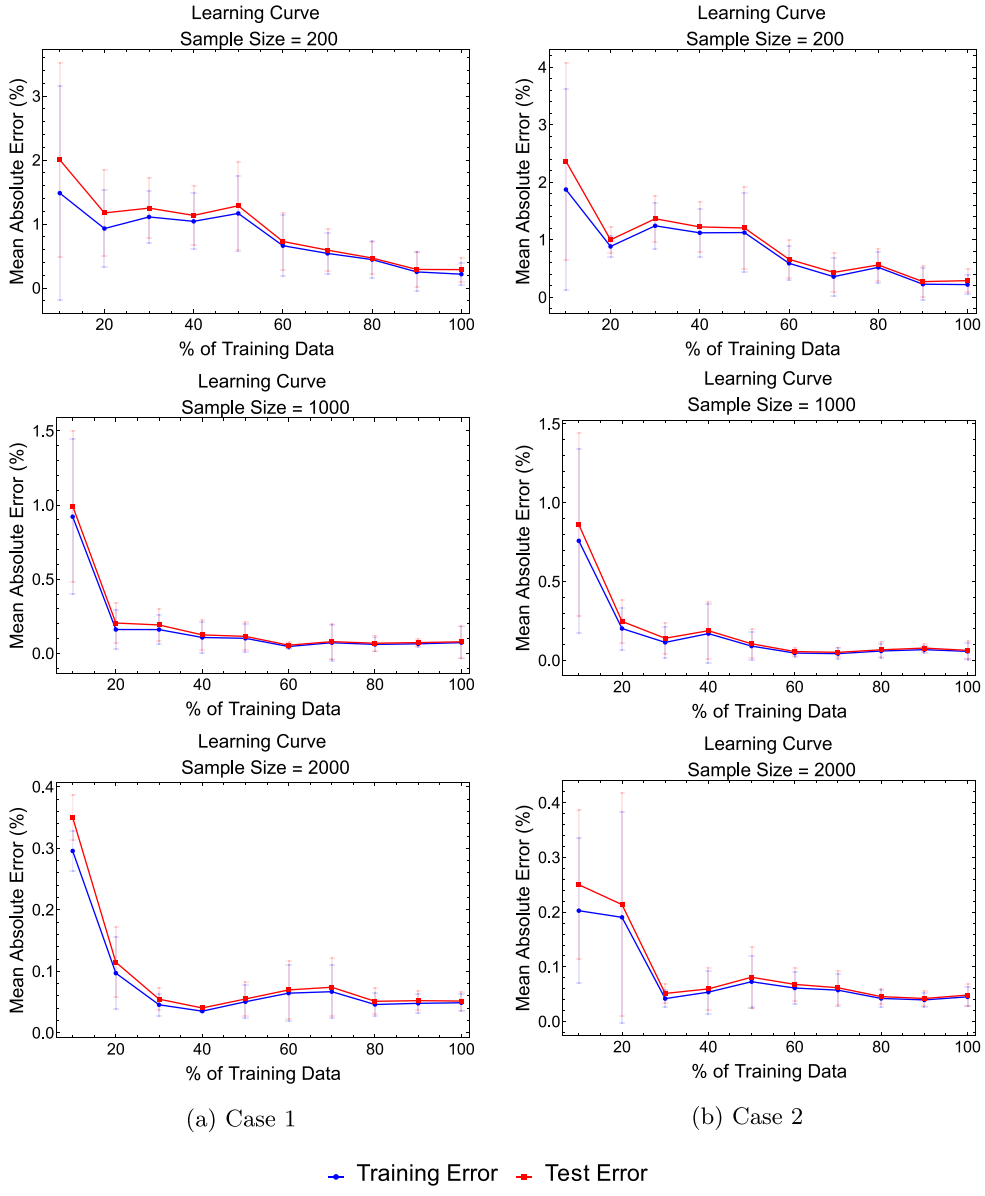

Fig. 7. Learning curves for Biot number estimation using Gradient Boosted Trees (GBT) under two base conditions: (a) Dirichlet and (b) Neumann.

6.3. Estimated parameter with simulated data

In order to evaluate the performance of the proposed estimation strategies for both considered boundary conditions, a parameter estimation was implemented using simulated data. This approach allows for controlled testing of the inverse methodologies. The primary goal involves assessing the accuracy and robustness of both classical and data-driven techniques in retrieving thermal parameters such as the Biot number. The simulated datasets employed in the following analysis, as previously described, incorporate measurement noise in order to emulate conditions that closely resemble experimental scenarios. Fig. 8 presents a comparative visualization of the temperature fields generated from the reference Biot number, the Levenberg–Marquardt (LM) estimation, and the Gradient Boosted Trees (GBT) prediction. These temperature distributions enable a qualitative assessment of the accuracy of each method with Biot number values of 0.01, 0.1 and 1.

It is important to mention that various initial guesses were tested for the LM code in order to determine its sensitivity to starting conditions. Even for initial guesses differing by more than 90% from the reference value were successful in estimating the Biot number in Case 1. For the considered results for Case 1, the visual comparison highlights the ability of both methods to approximate the reference solution, with the GBT offering performance comparable to the LM across all tested cases. In order to obtain a more quantitative analysis, an additional set of synthetic data corresponding to different Biot number values was generated. Thus, Fig. 9 presents a direct comparison between the reference values and those predicted by the Levenberg–Marquardt (LM) and Gradient Boosted Trees (GBT) method. The solid red line represents the fitted model, while the dashed red lines denote the ±10% relative error bounds. Points within these bounds correspond to estimates with less than 10% relative error. As can be inferred, both methods demonstrate good agreement with the reference values. The Gradient Boosted Trees (GBT) model achieves slightly higher accuracy for larger Biot numbers, whereas the Levenberg–Marquardt (LM) method yields lower errors for smaller Biot number values. A comparative analysis of the estimation accuracy reveals that the GBT method outperforms the LM approach, achieving an average relative error of 5.33% compared to 6.83% for LM. Although the LM method under Dirichlet boundary conditions exhibits reduced sensitivity to initial guesses — due to relatively stable residuals with respect to Biot number — it can

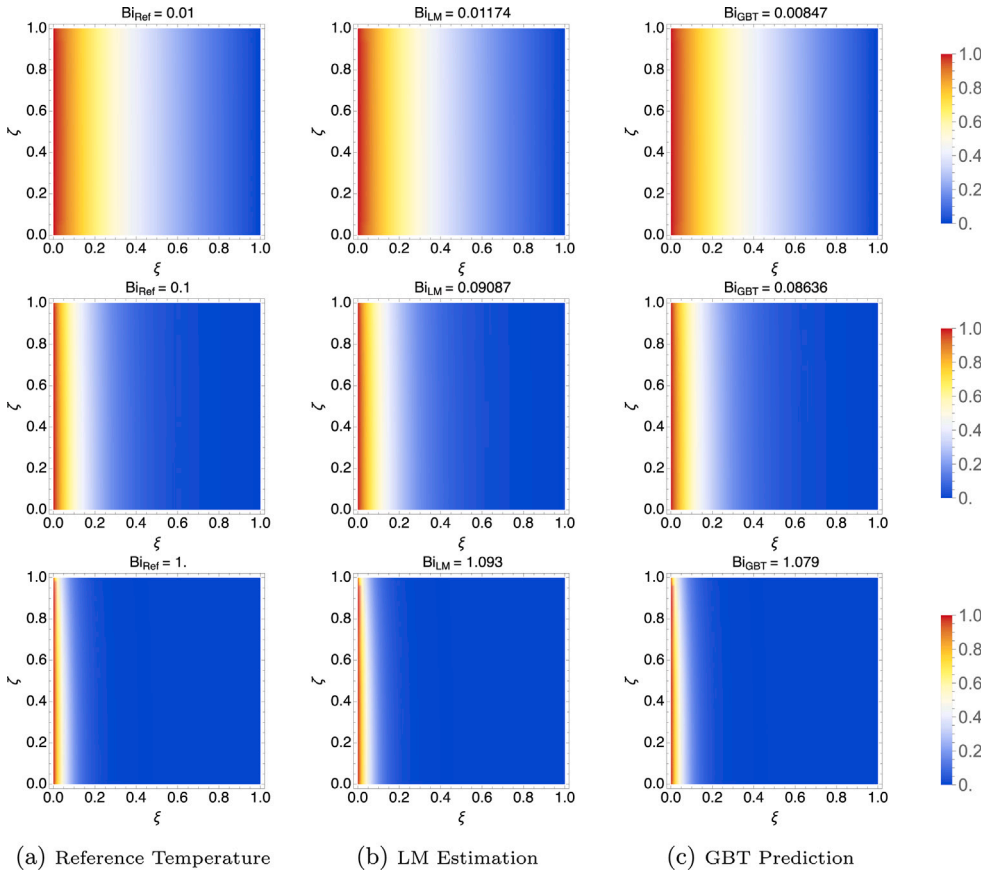

Fig. 8. Comparison of two-dimensional dimensionless temperature fields for different Biot numbers for Case 1. (a) shows the reference temperature distributions for Bi_{ref} = 0.01. 0.1 and 1; (b) shows the estimated temperature using the Levenberg–Marquardt (LM); and (c) presents those predicted by the Gradient Boosted Trees (GBT) model.

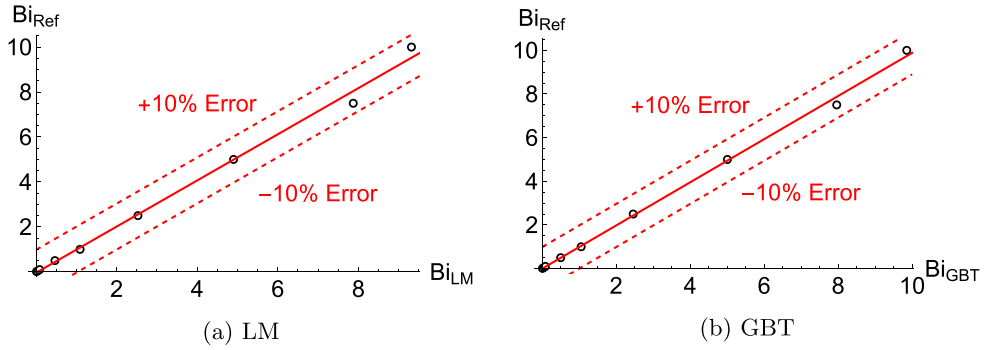

Fig. 9. Comparison for Case 1 between reference Biot numbers and estimated values obtained using (a) the Levenberg–Marquardt (LM) algorithm and (b) the Gradient Boosted Trees (GBT) model.

still encounter convergence challenges and fall into non-physical local minima. However, no such issues were observed in the present analysis. On the other hand, while the GBT can be more robust to measurement noise, its accuracy tends to degrade when estimating closely spaced Biot number values. This decline stems from the reduced sensitivity of the temperature field near the base for small Biot values, where profiles tend to become flatter and less distinguishable. This limitation was evident during training dataset verification, where various ranges and extremal values were examined.

As already perceived, for low Biot-values, the LM incorporates better estimates. In order to evaluate higher Biot numbers, for Case 2 with Neumann boundary condition at the base of the fin, Biot-values of 0.1, 1 and 10 are analyzed. Fig. 10 shows the comparison between reference heat flux streams and the estimated streams obtained using the Levenberg–Marquardt (LM) and Gradient Boosted Trees (GBT) methods for three different Biot numbers. Each subfigure shows the dimensionless heat flux along the fin, with contour colors indicating the vector fields representing the gradient direction. As one can observe, for Bi = 0.1, both methods show excellent agreement with the reference: the LM method estimates Bi = 0.1013, and GBT predicts Bi = 0.09227, both well within a 10% relative error.

For Bi = 1, the LM method slightly overestimates the reference value with Bi = 1.079, while GBT slightly underestimates it at Bi = 0.928. At the higher Biot number of 10, both methods approximate the target with reasonable accuracy; LM yields Bi = 12.08, and GBT predicts Bi = 9.765. Although the LM estimate shows a greater relative deviation in this case, the results demonstrate that both inverse techniques can reliably estimate the Biot number from experimental temperature data

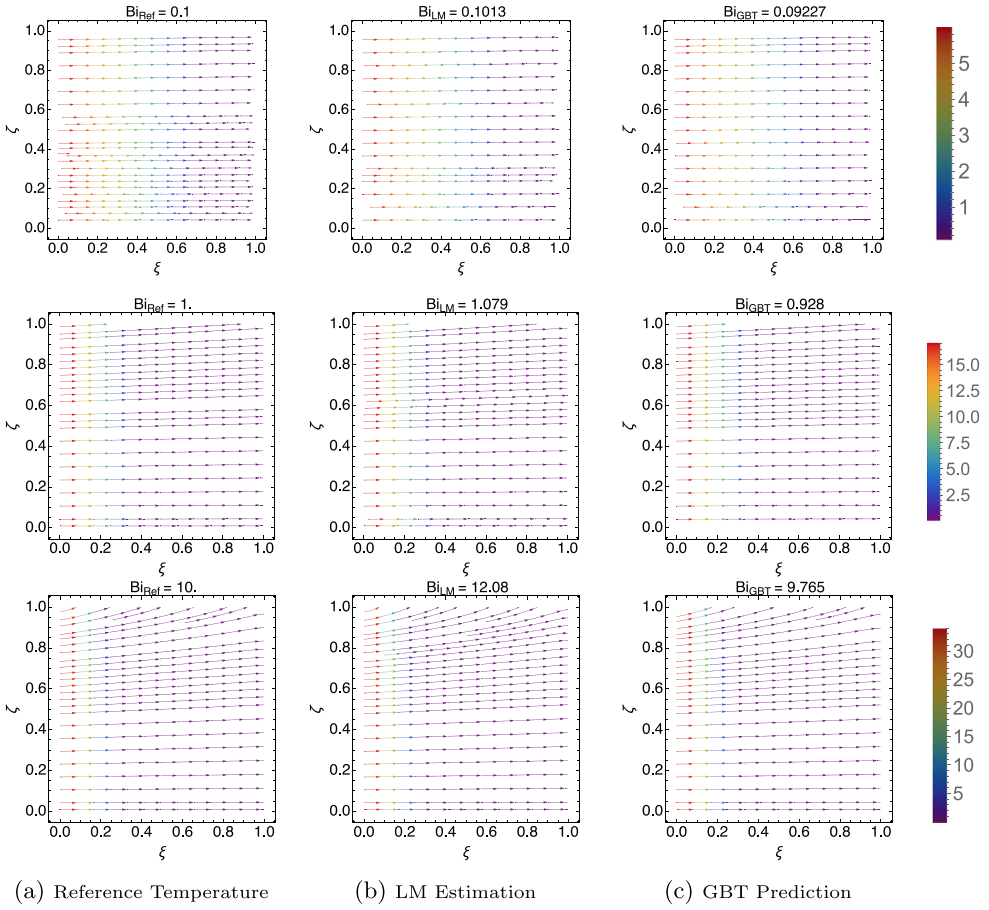

Fig. 10. Comparison of two-dimensional dimensionless heat flux for different Biot numbers for Case 2. (a) shows the reference temperature distributions for $Bi_{ref} = 0.1$. 1 and 10; (b) shows the estimated temperature using the Levenberg–Marquardt (LM); and (c) presents those predicted by the Gradient Boosted Trees (GBT) model.

— LM performing slightly better at lower Bi values and GBT exhibiting more stable performance across a broader range, as also seen in Case 1.

It is important to note that when the initial guess for the Biot number is relatively large, even a small perturbation can result in extremely small gradient values for the Neumann boundary condition. This leads to a near-singular Jacobian matrix, which compromises the quality of the gradient information required for the Levenberg–Marquardt (LM) method. As a consequence, the LM algorithm produces erratic/divergent updates, as it relied on unreliable directional cues from the sensitivity matrix. This issue was particularly evident under Neumann boundary conditions, where naturally the solution is more sensitive to noise and numerical instabilities. In such cases, proper tuning of the perturbation parameter ϵ_J becomes one of the essential steps in the numerical implementation to improve the stability and resolution of the Jacobian. Differently from Case 1 where all error and perturbation parameters were kept at 10^{-6}, in Case 2, higher values were implemented; however, it was still kept below 1%. Additionally, the Tikhonov regularization was implemented in this cases with $\lambda = 0.01$, which helped to suppress ill-conditioning and guided the solution away from non-physical regions in the parameter space, enabling a reliable convergence implementation.

Similarly to Case 1, Fig. 11 presents a direct comparison between the reference Biot numbers and those estimated using the Levenberg–Marquardt (LM) algorithm and the Gradient Boosted Trees (GBT) model. Each subplot includes a fitted solid red line, along with dashed red lines indicating ±10% relative error margins. As can be seen, in both comparisons, the majority of the estimated values fall within the ±10% bounds, demonstrating the overall reliability of both methods. The LM results show a slight overestimation trend for higher Biot numbers, especially above Bi = 8, although estimates for lower Bi values remain closely aligned with the reference. On the other hand, the GBT results exhibit more consistent behavior across the entire range, with a slightly better performance in high Bi situations. These observations align with the earlier quantitative error analysis, where the GBT achieved a lower maximum relative error of 5.4%, while the LM had an average error of 8.0%, where in some cases, the relative error was about 10% (For Bi = 7.5, for instance). Nonetheless, both methods prove effective in retrieving Biot numbers from temperature data, with their respective strengths depending on the Biot range considered.

After converting the dimensionless variables, the residuals were calculated in Celsius. The residuals were computed across both boundary condition cases in comparison with the simulated data for all Bi-values considered, highlighting the local discrepancies as a function of the longitudinal position x in millimeters. Overall, the residuals for both analysis are described in Fig. 12. As can be seen, the maximum residuals reveal that the values vary spatially along the fin, with fluctuations generally staying below 1°C in all cases. In Case 1, both methods present similar behavior with slightly lower and more stable residuals for the LM method compared to the GBT. In Case 2, residual magnitudes tend to be slightly lower overall, particularly for the GBT method, which appears more affected by measurement noise and spatial irregularities near the base. These results reinforce the observation that Dirichlet conditions yield more consistent parameter estimation performance, while Neumann conditions can amplify numerical instability and sensitivity to experimental fluctuations.

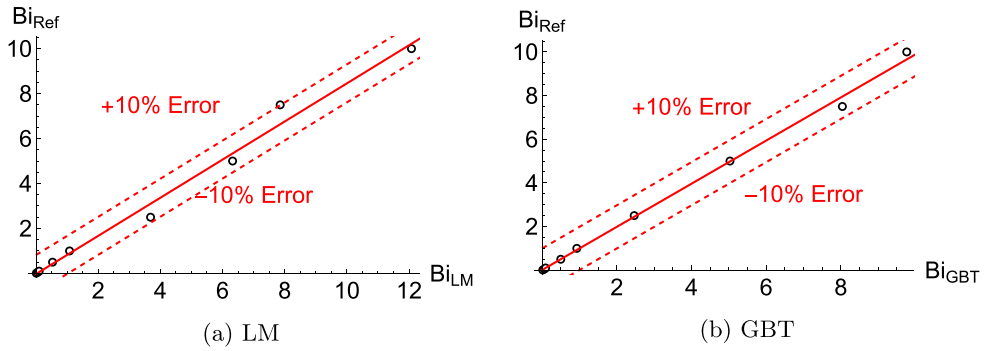

(a) LM (b) GBT

Fig. 11. Comparison for Case 2 between reference Biot numbers and estimated values obtained using (a) the Levenberg–Marquardt (LM) algorithm and (b) the Gradient Boosted Trees (GBT) model.

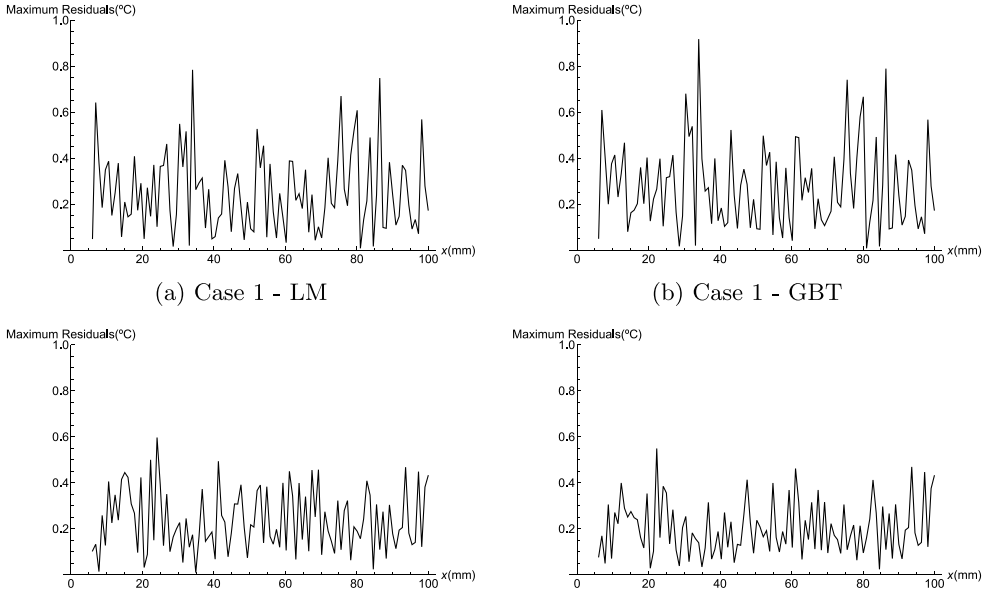

(a) Case 1 - LM (b) Case 1 - GBT

(c) Case 2 - LM (d) Case 2 - GBT

Fig. 12. Maximum residuals between the experimental and estimated temperature profiles along the fin for two boundary condition cases: (a) and (b) refer to Case 1 (Dirichlet condition at the base) using the Levenberg–Marquardt (LM) and Gradient Boosted Trees (GBT) methods, respectively, while (c) and (d) correspond to Case 2 (Neumann condition at the base)

Complementarily, Fig. 13 presents the spatial distribution of the sensitivity coefficients of the dimensionless surface temperature with respect to the Biot number, obtained from the finite-difference Jacobian employed in the LM algorithm, as seen in Eq. (18). The results compare Case 1 with an isothermal base (blue lines) and Case 2 with an isoflux base (red lines), using the same axial discretization along the fin length adopted in the inverse analysis. Sensitivity profiles are shown for Biot numbers Bi = 0.1, 1, and 10.

As can be seen, the analysis reveals a clear distinction between the two formulations in terms of sensitivity magnitude: although the sensitivity coefficients are negative in both cases, the Dirichlet formulation exhibits higher absolute values with a more pronounced peak, whereas the Neumann formulation presents lower sensitivity magnitudes that progressively decrease as the Biot number increases. The sensitivity information is strongly concentrated near the fin base and decays rapidly along the axial direction, indicating that the influence of the Biot number on the dimensionless temperature field is predominantly localized in this region, as expected. Despite the larger absolute sensitivities observed for the Dirichlet case, this information is highly localized and strongly constrained by the prescribed base temperature, particularly at low Biot numbers, where the thermal field becomes weakly dependent on convective effects. In contrast, under Neumann conditions the imposed heat flux allows the temperature field to respond more freely to variations in the Biot number at low Bi, distributing the sensitivity information more uniformly along the fin. However, for Bi = 10, the Neumann sensitivity coefficients approach zero over most of the domain, indicating that the temperature field becomes nearly insensitive to further changes in the Biot number. This loss of sensitivity reflects a saturation of the convective effect at the boundary and leads to a severely reduced information content for parameter estimation in this regime, emphasizing that identifiability is governed not only by sensitivity magnitude but also by its spatial persistence across the domain. Thus, under Neumann conditions, the progressive reduction of sensitivity magnitude at higher Bi reflects a weakening of the coupling between the thermal response and the Biot number, leading to reduced parameter identifiability in this regime, while the Dirichlet condition preserves a stronger sensitivity magnitude over a wider range of Bi.

The final comparison of Biot number estimations is presented in Tables 3 and 4, corresponding to isothermal and isoflux base conditions, respectively. These tables summarize the performance of two inverse methods — the Levenberg–Marquardt (LM) algorithm and the Gradient Boosted Trees (GBT) — across a range of reference Biot numbers (Bi = 0.01, 0.1, 1, and 10). As seen in Table 3, both methods

Table 3
Comparison of Biot number values for isothermal base at different reference Biot numbers.

Cases	Isothermal base							
Reference	Bi = 0.01	ϵ_r	Bi = 0.1	ϵ_r	Bi = 1	ϵ_r	Bi = 10	ϵ_r
Estimated by LM	0.01174	17.4%	0.09087	9.1%	1.09322	9.3%	9.31645	6.8%
Estimated by GBT	0.00847	15.3%	0.08636	13.6%	1.05395	5.4%	9.85432	1.5%

Table 4
Comparison of Biot number values for isoflux base at different reference Biot numbers.

Cases	Isoflux base							
Reference	Bi = 0.01	ϵ_r	Bi = 0.1	ϵ_r	Bi = 1	ϵ_r	Bi = 10	ϵ_r
Estimated by LM	0.01026	2.6%	0.10127	1.3%	1.07916	7.9%	12.07774	20.8%
Estimated by GBT	0.01684	6.8%	0.09227	7.7%	0.92803	7.2%	9.76488	2.4%

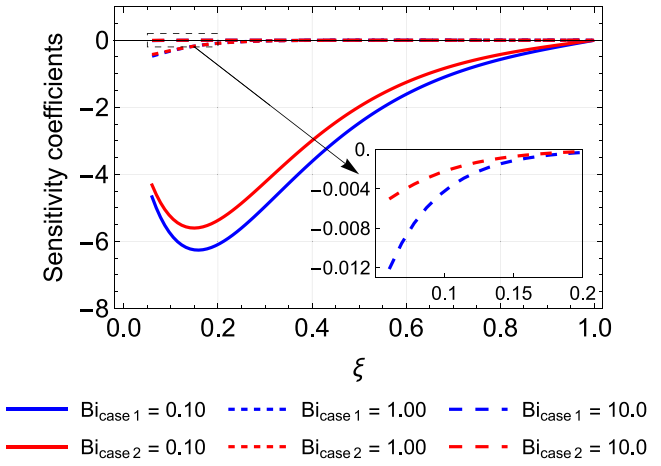

Fig. 13. Sensitivity coefficients with respect to the Biot number for Case 1 (blue lines) and Case 2 (red lines).

Table 5
Comparison of the Biot number (Bi) and the convective heat transfer coefficient h, estimated using the Levenberg–Marquardt (LM) algorithm and the Gradient Boosted Trees (GBT) model for isothermal (Dirichlet) base.

Cases	Isothermal base	
Estimated parameters	Bi	h
Estimated by LM	0.108 ± 0.037	3.978 ± 0.175
Estimated by GBT	0.191 ± 0.055	7.009 ± 0.134

Table 6
Comparison of the Biot number (Bi) and the convective heat transfer coefficient h, estimated using the Levenberg–Marquardt (LM) algorithm and the Gradient Boosted Trees (GBT) model for isoflux (Neumann) base.

Cases	Isoflux base	
Estimated parameters	Bi	h
Estimated by LM	0.108 ± 0.037	3.988 ± 0.144
Estimated by GBT	0.229 ± 0.055	8.418 ± 0.146

demonstrate strong agreement with reference values under isothermal boundary conditions, with only minor deviations that become more pronounced at higher Biot numbers. A similar pattern is observed in Table 4, where slightly larger deviations occur, particularly for the LM method at Bi = 10 under isoflux conditions. These results underscore the strengths and limitations of each technique across different thermal boundary scenarios. The GBT generally provides higher accuracy at elevated Biot numbers due to its robustness in resolving steep thermal gradients near boundaries, which is an advantage that depends heavily on the availability of well-sampled and representative training data. Poorly sampled datasets can compromise the GBT's generalization capability, especially when extrapolating beyond the training domain. Moreover, the GBT is more sensitive to measurement noise and requires carefully selected training conditions to ensure reliable convergence. In contrast, the LM method, while widely effective in inverse problems, depends on proper regularization to manage the ill-posed nature of parameter estimation. Without adequate regularization, the LM may experience instability, slow convergence, or reduced accuracy, particularly under strong nonlinearities or when the parameter space is poorly conditioned.

Ultimately, neither the GBT nor the LM method can be deemed universally superior — their effectiveness is context-dependent. GBT tends to excel in complex, nonlinear regimes such as high Biot number scenarios, provided that high-quality, representative training data are available. Conversely, the LM method is more appropriate in settings where analytical sensitivity is accessible and effective regularization can be applied. Therefore, the selection between these approaches should be guided by the nature of the available data, the complexity of the inverse problem, and the stability requirements of the solution.

6.4. Estimated parameter with experimental data

This section presents the results of the parameter estimation using experimental temperature data obtained through infrared thermography. The inverse analysis was conducted using both the Levenberg–Marquardt (LM) algorithm and the Gradient Boosted Trees (GBT) method, aiming to determine the Biot number that best fits the measured temperature distributions. Prior to the estimation, the experimental data were pre-processed and aligned with the spatial domain of the numerical model. The results are analyzed in terms of confidence intervals and consistency with reference values, allowing a comparison between the performance and robustness of both estimation approaches when applied to real, noise-affected data, as can be visualized in Fig. 14. For both cases, the x-axis represents the longitudinal position along the fin, and the y-axis denotes the temperature in degrees Celsius. The black dashed line corresponds to the fitted reference profile, while the green and red lines represent the LM and GBT estimates, respectively. The shaded blue region indicates the 95% confidence interval (CI) for the experimental measurements. As can be seen, in Case 1 (Dirichlet condition at the base), both the LM and the GBT estimations closely follow the fitted curve within the confidence bounds, with the GBT showing slightly better alignment throughout the domain. In Case 2 (Neumann condition at the base), the discrepancy between the LM and the fitted profile is more evident near the base, indicating a reduced sensitivity of the model to Biot number variations under this boundary condition. Despite this, both methods remain within the 95% CI, validating their applicability even in the presence of greater uncertainty in the measured data.

Table 5 presents the estimated Biot numbers and convective coefficients h obtained using the Levenberg–Marquardt (LM) and Gradient Boosted Trees (GBT) methods for Case 1, while Table 6 presents the

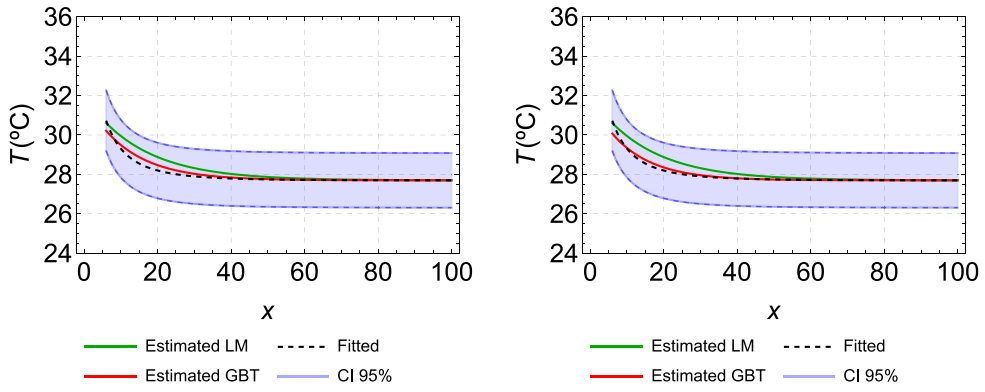

Fig. 14. Comparison of temperature distributions estimated by the Levenberg–Marquardt (LM) algorithm and Gradient Boosted Trees (GBT) model against the fitted temperature profile for two boundary condition cases.

same results for Case 2. The results are shown for both isothermal (Dirichlet) and isoflux (Neumann) boundary conditions at the base of the fin. As observed, for the isothermal base, both methods yield close Biot number values, with the LM estimating Bi = 0.10822 and the GBT estimating a higher value of Bi = 0.19066. This difference leads to corresponding estimates of h as 3.97818 and 7.00868, respectively. For the isoflux base, the LM method again yields a lower Biot number (0.10848) compared to GBT (0.22900), with the estimated h values increasing accordingly. The GBT model tends to estimate higher Bi and h values under both boundary conditions, which may reflect its greater sensitivity to small variations in the temperature profile, especially in regions where the gradient is less pronounced. These differences highlight how the choice of estimation method and boundary condition influences the inferred thermal parameters.

The results reveal important contrasts between the two estimation methods and boundary conditions. The Levenberg–Marquardt algorithm demonstrated high sensitivity to initial guesses, particularly in Case 2 (Neumann condition), where an initial value far from the true Biot number often led to instability due to irregular or near-zero partial derivatives of the temperature field with respect to Biot. This behavior compromises the conditioning of the Jacobian matrix, resulting in poor update directions or even divergence. Nevertheless, when the initial guess was close to the correct value, Case 2 provided better identifiability and convergence than Case 1, as the Neumann condition amplifies the surface sensitivity of the model, especially near the base. In contrast, the Gradient Boosted Trees model proved more robust to initial input variation but suffered from reduced accuracy when the training data lacked sufficient resolution around the true Biot number, particularly under the isoflux condition. Overall, while Case 1 offers more stable performance for LM under limited data, Case 2 presents superior sensitivity and convergence characteristics when appropriately initialized or when data coverage is sufficient, reinforcing its utility in inverse parameter identification problems.

From the experimental analysis, it can be inferred that the Levenberg–Marquardt method provides accurate and physically consistent estimates of the Biot number when the temperature field exhibits sufficient sensitivity to the parameter, as observed primarily under Dirichlet base boundary conditions. In these cases, the physically grounded formulation, combined with appropriate regularization, yields stable, convergent, and interpretable solutions. On the other hand, the Gradient Boosted Trees approach exhibits enhanced robustness to measurement noise and reduced sensitivity regimes, providing estimates that are, on average, closer to the experimental data, particularly under Neumann boundary conditions where gradient-based information becomes weak. Therefore, for the experimental case analyzed herein, the regularized classical inverse method remains a reliable and interpretable tool when favorable sensitivity conditions are present, while the machine learning approach offers superior robustness and complementary accuracy in scenarios characterized by lower identifiability or higher experimental uncertainty.

7. Conclusions

This study presented a unified framework integrating infrared thermography, analytical modeling via integral transforms, and two distinct inverse estimation approaches — Levenberg–Marquardt (LM) and Gradient Boosted Trees (GBT) — to determine the Biot number in polymeric fins under both Dirichlet (temperature-controlled) and Neumann (flux-controlled) base conditions. A dimensionless steady-state heat conduction model was employed with two boundary conditions at the base — prescribed temperature (Dirichlet) and prescribed heat flux (Neumann) — allowing for a comparative analysis of their influence on the identifiability and stability of inverse solutions. Synthetic datasets generated from the analytical solutions enabled a systematic evaluation of each method's performance. Infrared thermographic measurements from acrylic samples served as the experimental benchmark, enabling validation of the predictive capacity of each estimation approach.

The LM method demonstrated reliable performance for lower Biot number values, particularly under Dirichlet boundary conditions, benefiting from the regularization strategies implemented to address the inherent ill-posedness of the inverse problem. These strategies, which are based on scaled damping and reference-guided penalization, were essential to stabilize the parameter estimation process and improve convergence. However, in scenarios involving Neumann boundary conditions, LM encountered limitations due to sensitivity matrix ill-conditioning, particularly at high Biot number values.

On the other hand, the GBT method showed higher accuracy and robustness across a broader Biot number range, especially at higher values. Its performance benefits from enhanced pattern recognition in strongly nonlinear regimes and reduced sensitivity to noise. Nevertheless, the effectiveness of the GBT model depends heavily on the quality and diversity of the synthetic training data. Poorly sampled datasets or insufficient representation of low-gradient regions can lead to reduced resolution and estimation uncertainty.

Ultimately, the appropriate choice between LM and GBT depends on the problem context: the LM offers interpretability and strong performance where sensitivity conditions are favorable, while the GBT is preferable in complex, nonlinear scenarios with sufficient training data. These findings reinforce the complementary nature of classical inverse methods and machine learning strategies in thermal parameter estimation.

CRediT authorship contribution statement

Isabela Florindo Pinheiro: Writing – review & editing, Visualization, Validation, Software, Methodology, Investigation, Formal analysis, Data curation. **Debora Carneiro Moreira:** Writing – original draft, Visualization, Validation, Data curation, Conceptualization. **Daniel Pereira Nunes Gama:** Writing – review & editing, Visualization, Investigation, Formal analysis. **Leandro Alcoforado Sphaier:** Writing – original draft, Supervision, Resources, Project administration, Methodology, Funding acquisition, Formal analysis, Conceptualization. **Luiz Carlos da Silva Nunes:** Writing – original draft, Supervision, Resources, Funding acquisition, Formal analysis, Data curation, Conceptualization.

Declaration of competing interest

The authors declare that they have no known competing financial interests or personal relationships that could have appeared to influence the work reported in this paper.

Acknowledgments

The authors are grateful for the financial support offered by the Brazilian Government agencies CNPq, CAPES, Brazil, ANP, Brazil and FAPERJ, Brazil (Grants numbers E-26/204.503/2022 and E-26/200.261/2023).

Data availability

Data will be made available on request.

References

[1] T. Astarita, G. Cardone, G. Carlomagno, C. Meola, A survey on infrared thermography for convective heat transfer measurements, Opt. Laser Technol. 32 (7) (2000) 593–610.
[2] M. Clark, D. McCann, M. Forde, Application of infrared thermography to the non-destructive testing of concrete and masonry bridges, Ndt E Int. 36 (4) (2003) 265–275.
[3] J. Iljaž, L. Wrobel, T. Gomboc, M. Hriberšek, J. Marn, Solving inverse bioheat problems of skin tumour identification by dynamic thermography, Inverse Problems 36 (3) (2020) 035002.
[4] G.M. Carlomagno, G. Cardone, Infrared thermography for convective heat transfer measurements, Exp. Fluids 49 (6) (2010) 1187–1218.
[5] T. Astarita, G. Cardone, G. Carlomagno, Infrared thermography: An optical method in heat transfer and fluid flow visualisation, Opt. Lasers Eng. 44 (3) (2006) 261–281.
[6] C. Balaras, A. Argiriou, Infrared thermography for building diagnostics, Energy Build. 34 (2) (2002) 171–183.
[7] P. Song, A. Trivedi, C.R. Siviour, Tensile testing of polymers: Integration of digital image correlation, infrared thermography and finite element modelling, J. Mech. Phys. Solids 171 (2023) 105161.
[8] N. Moslemi, B. Abdi, S. Gohery, I. Sudin, E. Atashpaz-Gargari, N. Redzuan, A. Ayob, C. Burvill, M. Su, F. Arya, Thermal response analysis and parameter prediction of additively manufactured polymers, Appl. Therm. Eng. 212 (2022) 118533.
[9] D.C. Knupp, Integral transform technique for the direct identification of thermal conductivity and thermal capacity in heterogeneous media, Int. J. Heat Mass Transfer 171 (2021) 121120.
[10] C.P. Naveira-Cotta, R.M. Cotta, H.R. Orlande, Inverse analysis with integral transformed temperature fields: Identification of thermophysical properties in heterogeneous media, Int. J. Heat Mass Transfer 54 (7–8) (2011) 1506–1519, http://dx.doi.org/10.1016/j.ijheatmasstransfer.2010.11.042.
[11] M. Asif, A. Tariq, K.M. Singh, Estimation of thermal contact conductance using transient approach with inverse heat conduction problem, Heat Mass Transf. 55 (2019) 3243–3264.
[12] W.-L. Chen, H.-M. Chou, Y.-C. Yang, An inverse problem in estimating the space-dependent thermal conductivity of a functionally graded hollow cylinder, Compos. Part B: Eng. 50 (2013) 112–119.
[13] F. Mohebbi, B. Evans, A. Shaw, M. Sellier, An inverse analysis for determination of space-dependent heat flux in heat conduction problems in the presence of variable thermal conductivity, Int. J. Comput. Methods Eng. Sci. Mech. 20 (3) (2019) 229–241.
[14] C. Pacheco, H. Orlande, M. Colaço, G. Dulikravich, Real-time identification of a high-magnitude boundary heat flux on a plate, Inverse Probl. Sci. Eng. 24 (9) (2016) 1661–1679.
[15] I. Pinheiro, G. Puccetti, G. Morini, L. Sphaier, Integral transform analysis of microchannel fluid flow: Irregular geometry estimation using velocimetry data, Appl. Math. Model. 90 (2021) 943–954.
[16] J.F.L. Sousa, S. Lavagnoli, G. Paniagua, L. Villafañe, Three-dimensional (3D) inverse heat flux evaluation based on infrared thermography, Quant. InfraRed Thermogr. J. 9 (2) (2012) 177–191.
[17] H. Liu, C. Pei, S. Xie, Y. Li, Y. Zhao, Z. Chen, Inversion technique for quantitative infrared thermography evaluation of delamination defects in multilayered structures, IEEE Trans. Ind. Inform. 16 (7) (2019) 4592–4602.
[18] V.F. Egger, M.Z.M. Bria, K.M. Lisboa, K.D.A. Da Costa, C.C. Pacheco, I.F. Pinheiro, Experimental investigation and Kalman filter-based estimation of spatial-dependent heat sources in microprocessor hotspots, J. Braz. Soc. Mech. Sci. Eng. 47 (2) (2025/01/15) 74, http://dx.doi.org/10.1007/s40430-024-05369-w.
[19] F. Bozzoli, L. Cattani, A. Mocerino, S. Rainieri, I. Tougri, M. Colaço, Characterisation of the heat transfer in displaced enhancement devices by means of inverse problem approach applied to IR images, Quant. InfraRed Thermogr. J. 18 (2) (2021) 108–126.
[20] E.L. Sanches, D.C. Knupp, L.T. Stutz, L.A. Abreu, A.J.S. Neto, Use of infrared thermography for the explicit heat flux estimation employing regularized measurements with truncated eigenfunction expansions, Therm. Sci. Eng. Prog. 26 (2021) 101084.
[21] S. Chudzik, Measurement of thermal parameters of a heat insulating material using infrared thermography, Infrared Phys. Technol. 55 (1) (2012) 73–83.
[22] S. Chudzik, Applying infrared measurements in a measuring system for determining thermal parameters of thermal insulation materials, Infrared Phys. Technol. 81 (2017) 296–304.
[23] F. Mohebbi, M. Sellier, Parameter estimation in heat conduction using a two-dimensional inverse analysis, Int. J. Comput. Methods Eng. Sci. Mech. 17 (4) (2016) 274–287.
[24] C. Le Niliot, P. Gallet, Infrared thermography applied to the resolution of inverse heat conduction problems: recovery of heat line sources and boundary conditions, Rev. GénÉrale Therm. 37 (8) (1998) 629–643.
[25] C.-H. Huang, K.-C. Fang, An inverse problem for estimating spatially and temporally dependent surface heat flux with thermography techniques, Mathematics 12 (10) (2024) 1584.
[26] J.-G. Bauzin, S. Vintrou, N. Laraqi, 3D-transient identification of surface heat sources through infrared thermography measurements on the rear face, Int. J. Therm. Sci. 148 (2020) 106115.
[27] S. Somasundharam, K. Reddy, Simultaneous estimation of thermal properties of orthotropic material with non-intrusive measurement, Int. J. Heat Mass Transfer 126 (2018) 1162–1177.
[28] T. Helmig, T. Göttlich, R. Kneer, An infrared thermography based experimental method to quantify multiscale thermal resistances at non-conforming interfaces, Int. J. Heat Mass Transfer 186 (2022) 122399.
[29] P. Millan, Resolution of a three-dimensional unsteady inverse problem by sequential method using parameter reduction and infrared thermography measurements, Numer. Heat Transf.: Part A: Appl. 37 (6) (2000) 587–611.
[30] F. Zhu, J. Chen, Y. Han, D. Ren, A deep learning method for estimating thermal boundary condition parameters in transient inverse heat transfer problem, Int. J. Heat Mass Transfer 194 (2022) 123089.
[31] A. Sarhadi, R.Q. Albuquerque, M. Demleitner, H. Ruckdäschel, M.A. Eder, Machine learning based thermal imaging damage detection in glass-epoxy composite materials, Compos. Struct. 295 (2022) 115786.
[32] J. Jo, Y. Jeong, J. Kim, J. Yoo, Thermal conductivity estimation using physics-informed neural networks with limited data, Eng. Appl. Artif. Intell. 137 (2024) 109079.
[33] S. Cai, Z. Wang, S. Wang, P. Perdikaris, G.E. Karniadakis, Physics-informed neural networks for heat transfer problems, J. Heat Transf. 143 (6) (2021) 060801.
[34] D.C. Moreira, M.C.O. Telles, L.A. Sphaier, L.C.S. Nunes, Infrared thermography for estimating the thermal conductivity augmentation of polymeric nanocomposites, High Temp. - High Press. 44 (1) (2015) 3–23.
[35] M. Colaco, H. Orlande, Inverse forced convection problem of simultaneous estimation of two boundary heat fluxes in irregularly shaped channels, Numer. Heat Transf.: Part A: Appl. 39 (7) (2001) 737–760.
[36] M.J. Colaço, H.R. Orlande, Inverse convection problems in irregular geometries, in: Proc. of the 21st Southeastern Conference on Theoretical and Applied Mechanics, Orlando, Florida, USA, 2002.
[37] M.J. Colaço, H.R. Orlande, G.S. Dulikravich, F.A. Rodrigues, A comparison of two solution techniques for the inverse problem of simultaneously estimating the spatial variations of diffusion coefficients and source terms, in: ASME 2003 International Mechanical Engineering Congress and Exposition, American Society of Mechanical Engineers, 2003, pp. 221–230.
[38] M.J. Colaço, H.R.B. Orlande, G.S. Dulikravich, Inverse and optimization problems in heat transfer, J. Braz. Soc. Mech. Sci. Eng. 28 (2006) 1–24.
[39] G. Dulikravich, T. Martin, Inverse shape and boundary condition problems and optimization in heat conduction, Adv. Numer. Heat Transf. 1 (1996) 381–426.

[40] J.P. Kaipio, C. Fox, The Bayesian framework for inverse problems in heat transfer, Heat Transf. Eng. 32 (9) (2011) 718–753.
[41] H. Machado, H. Orlande, Inverse analysis for estimating the timewise and spacewise variation of the wall heat flux in a parallel plate channel, Internat. J. Numer. Methods Heat Fluid Flow 7 (7) (1997) 696–710, http://dx.doi.org/10.1108/09615539710185578.
[42] C.A. Mota, H.R. Orlande, O. Wellele, V. Kolehmainen, J. Kaipio, Inverse problem of simultaneous identification of thermophysical properties and boundary heat flux, High Temp.–High Press 38 (2009) 171–185.
[43] H.R. Orlande, Inverse problems in heat transfer: new trends on solution methodologies and applications, J. Heat Transf. 134 (3) (2012) 031011.
[44] P.C. Sabatier, Applied inverse problems, in: Applied Inverse Problems, vol. 85, 1978.
[45] D.C. Moreira, M.C.O. Telles, L.C.S. Nunes, L.A. Sphaier, Analysis of improved-lumped models for property estimation from temperature field data using a fin model, J. Porous Media 18 (10) (2015).
[46] M.D. Mikhailov, M.N. Özisik, Unified Analysis and Solutions of Heat and Mass Diffusion, Courier Dover Publications, New York, 1984,
[47] K. Levenberg, A method for the solution of certain nonlinear problems in least squares, Quart. Appl. Math. 2 (1944) 164—168.
[48] D.W. Marquardt, An algorithm for least-squares estimation of nonlinear parameters, J. Soc. Ind. Appl. Math. 11 (2) (1963) 431–441.
[49] A.N. Tikhonov, V.Y. Arsenin, Solutions of ill-posed problems, in: Halsted Press book, Vh Winston, Michigan, 1977.
[50] O. Alifanov, Determination of heat loads from a solution of non-linear inverse problem, High Temp. 15 (3) (1977) 498–504.
[51] O. Alifanov, Inverse Heat Transfer Problems, Springer-Verlag, NewYork, 1994.
[52] J.V. Beck, K.J. Arnold, Parameter Estimation in Engineering and Science, Wiley, New York, 1977.
[53] J.V. Beck, K.A. Woodbury, Inverse problems and parameter estimation: integration of measurements and analysis, Meas. Sci. Technol. 9 (6) (1998) 839.
[54] M.N. Özışık, H. Orlande, Inverse Heat Transfer: Fundamentals and Applications, Taylor and Francis, New York, 2000.
[55] S. Wolfram, The Mathematica Book, fifth ed., Wolfram Media/Cambridge University Press, New York/Champaign, IL, 2003.